Mean Meridional Circulation in the Southern Hemisphere Stratosphere during the Polar Night

By

Robert F. Adler

Department of Atmospheric Science
Colorado State University
Fort Collins, Colorado

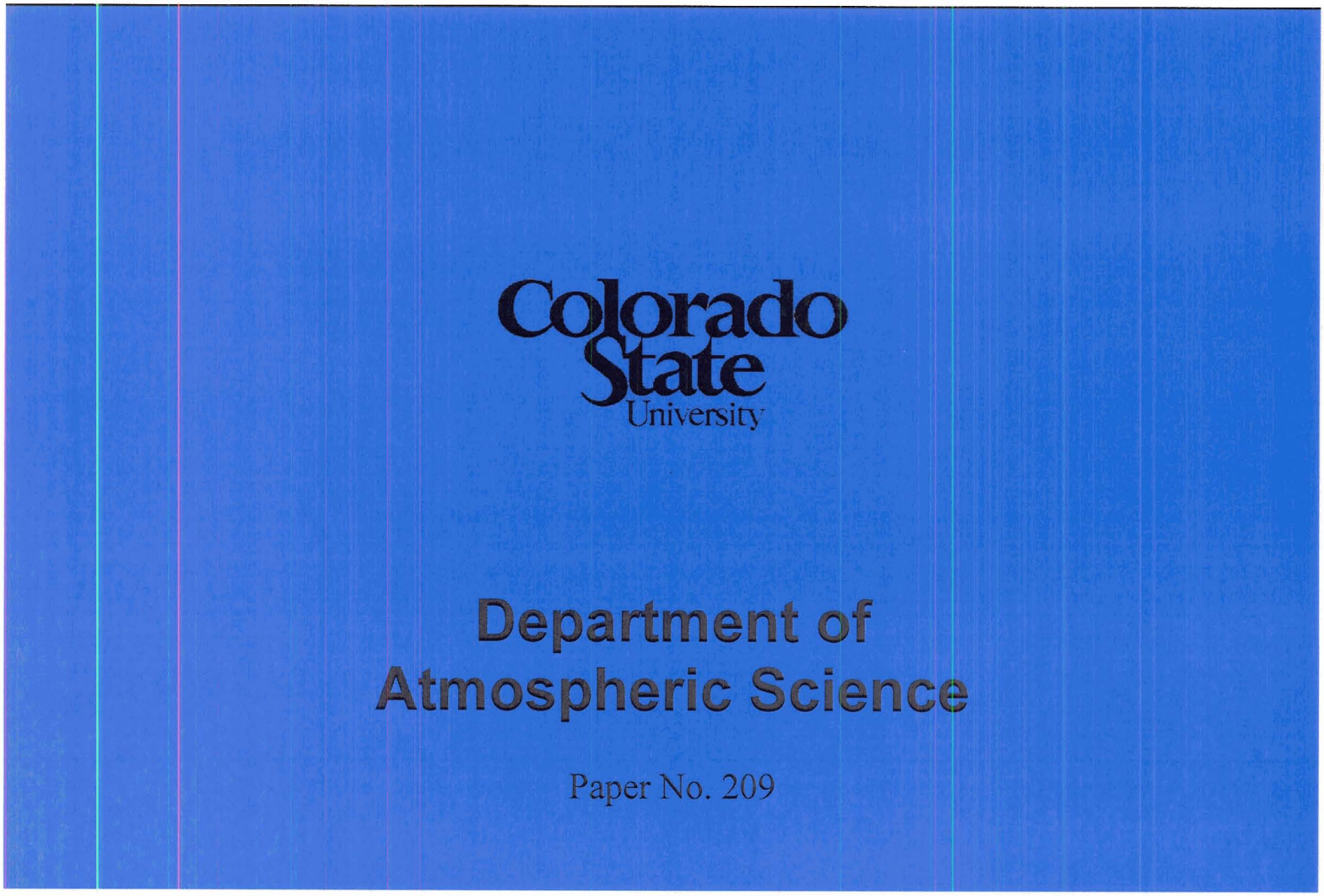

MEAN MERIDIONAL CIRCULATION IN THE SOUTHERN HEMISPHERE STRATOSPHERE DURING THE POLAR NIGHT

by

Robert F. Adler

This report was prepared with support from

NASA Grant No. NGR 06-002-098

Principal Investigator: Elmar R. Reiter

Department of Atmospheric Science

Colorado State University

Fort Collins, Colorado

November 1973

Atmospheric Science Paper No. 209

Abstract

Atmospheric structure derived from satellite, multi-channel radiance data is used to calculate zonally-averaged vertical motions in the wintertime stratosphere of both hemispheres. The Northern Hemisphere calculations confirm the two-celled meridional circulation calculated by previous authors. The Southern Hemisphere results show a three-celled structure with descending motion over the South Pole. The variability of the mean meridional circulation in the Southern Hemisphere in relation to the presence or absence of a minor midwinter warming is also discussed.

TABLE OF CONTENTS

1. Introduction

A number of studies (Reed, Wolfe and Nishimoto, 1963; Mahlman, 1966; Julian and Libitzke, 1965) have shown that the mean meridional circulation in the lower half of the stratosphere in the Northern Hemisphere winter has a two-celled structure with rising motion in low latitudes and over the pole and sinking motion in mid-latitudes. This zonally-averaged vertical motion pattern exists before, during and after mid-winter breakdowns of the polar vortex (Mahlman, 1966). In the Southern Hemisphere the mean meridional circulation is practically unknown. Rubin and Weyant (1963) do indicate a sinking motion over the pole below 75 mb. Also Reiter (1969, 1971) on the basis of ozone measurements over Antarctica, postulates a general sinking motion over the pole in the stratosphere. No evidence is available in the literature regarding the mean meridional circulation outside the southern polar regions.

The primary reason for the lack of information concerning the mean meridional motion in the Southern Hemisphere stratosphere is, of course, the lack of a substantial radiosonde network in the Southern Hemisphere. The lack of data precludes daily analysis of the stratosphere from conventional data alone. In the past few years, however, data has become available from satellite, multi-channel infrared radiometers such as the Satellite Infrared Spectrometer (SIRS). Techniques have been developed to obtain atmospheric temperature profiles from such data (see, for example an aritcle by Smith, Woolf and Jacob, 1970). Using such temperature retrieval techniques one can obtain daily hemispheric analyses of temperature structure at various levels. In this study temperature and geopotential height information is obtained from Nimbus 3 SIRS data. The atmospheric structure so obtained is used as a basis

for a computation of the zonally-averaged vertical motion patterns during winter months in both hemispheres. In the Northern Hemisphere the calculations are also carried out using the data fields of the National Meteorological Center (NMC).

2. Method used to obtain atmospheric structure from Nimbus 3 SIRS radiances

In this study thickness or temperature information is determined from the SIRS data by a regression technique. A linear, step-wise, least squared error, multiple regression technique is used. The dependent variables in the regression procedure are the thicknesses for the following layers: 1000-700 mb, 700-500 mb, 500-300 mb, 300-200 mb, 200-100 mb, 100-50 mb, 50-30 mb and 30-10 mb. The independent variables are the radiances of the eight SIRS channels. Separate regression equations are determined for each layer and for each of the following latitude zones: 20-40°, 40-60° and 60-80°.

The regression technique is based on a comparison of thickness information and cloud-free radiance data. When the regression equations derived from the comparison are applied to other radiance data, only cloud-free data are used. To eliminate cloud-contaminated data from the comparison data set and from the application of the regression equations, a simple, objective "cloud check" procedure is used. The "cloud check" procedure is based solely on the satellite radiance information.

The SIRS channels with weighting function peaks in the low troposphere (channels 1 through 3) are most affected by the presence of clouds. Channels with weighting function peaks in the stratosphere (channels 7 and 8) are only rarely affected by the presence of

tropospheric clouds. The radiance in the window channel (channel 1, $k=899cm^{-1}$) in the absence of clouds is related to the surface temperature. In the presence of an overcast, the channel 1 radiance is a function of cloud-top temperature, which is, of course, lower than the surface temperature. Therefore, channel 1 radiances much below normal would indicate the presence of clouds. However, the radiance in channel 1 is highly variable even in the absence of clouds because of its dependence on the surface temperature. Large changes in channel 1 radiance occur along satellite tracks in the presence of sharp changes in surface characteristics. This is especially true along land-sea boundaries. Also, large diurnal changes are present in the channel 1 radiance because of large changes in surface temperature. Channels 2 and 3 are also affected by clouds, but are not so severely affected by surface characteristics as channel 1. Therefore, channels 2 and 3 are used for the "cloud check."

SIRS radiance data is eliminated as being cloud-contaminated when the observed radiance in both channels 2 and 3 is below critical values. The critical values for both channels are determined by a comparison of SIRS data and satellite video data and are a function of latitude and season. Any data with both channel 2 and 3 radiances below the critical levels are eliminated as cloud-contaminated. The "cloud check" procedure is simple and certainly not foolproof. Some slightly cloud-contaminated data may still find their way into the final data set. The procedure as outlined above removes, on the average, about 15 percent of the original data points.

To obtain the regression coefficients, comparison sets of radiance and thickness data are developed. The observations are near-simultaneous

and at, or close to, the same geographic position. Somewhat different techniques are used for the Northern Hemisphere and the Southern Hemisphere. In the Northern Hemisphere, for the layer 100 to 1000 mb, the SIRS radiance data is matched with the National Meteorological Center (NMC) Northern Hemisphere fields. For satellite data occurring within three hours of NMC map time, the NMC grid point data is linearly interpolated to the satellite track position. For the layers above 100 mb, station data is matched with the satellite radiance information. The station location must be within 180 nautical miles of the satellite position, and the satellite observation time must be within three hours of the station observation time.

In the Southern Hemisphere, a different technique is used. Station data is matched with satellite radiance data for all levels. Because of the relative lack of stations in the Southern Hemisphere and the need for a sufficient number of data points for the regression analysis, the matchup restrictions are somewhat relaxed from those in the Northern Hemisphere. For each 24-hour period surrounding the 0000 GMT and 1200 GMT radiosonde times, all radiance data is placed into a five degree latitude by five degree longitude grid for the latitudes 20°S to 80°S. The radiance fields are analyzed and the radiances in each of the eight channels are linearly interpolated from the gridded data to the station locations. The data match-up is restricted to times and locations when there is original satellite data within a geographic box 600 nautical miles on a side surrounding the station. This technique is used for all levels.

The selection of the regression equations to be used in computing thicknesses is based on certain statistical and practical criteria. The

step-wise, multiple regression technique uses an F test to determine if additional independent variables should be introduced into the particular regression under consideration. In addition, the number of independent variables is restricted to a maximum of four. Most of the regression equations have three independent variables; however, a few have less than three. The standard error of estimate for each of the eight layers is given in Table 1 for each hemisphere. These statistics are for the three latitude bands combined (area weighted), and are for the dependent data on which the regression equations are based.

No regression equations could be determined for the 10-30 mb layer in the Southern Hemisphere because of a complete lack of data above 30 mb. In the analysis that follows the Northern Hemisphere 10-30 mb regression equations are applied to the Southern Hemisphere radiances to produce thickness fields in the 10-30 mb layer in the Southern Hemisphere.

	N. H Jan 70	S. H July 69
10-30 mb	2.1° C	
30-50 mb	3.0	1.7° C
50-100 mb	2.3	1.7
100-200 mb	2.0	1.9
200-300 mb	2.4	2.3
300-500 mb	2.8	2.3
500-700 mb	3.5	2.8
700-1000 mb	5.2	3.2

Table 1. Hemispheric standard errors of estimate for thickness regression equations

Geopotential heights for the SIRS-based data set are determined by summing the satellite-based thicknesses from a conventional 1000 mb height field. In the Northern Hemisphere the NMC 1200 GMT 1000 mb height fields are used. In the Southern Hemisphere 1000 mb height fields are obtained by converting daily surface pressure analyses of the Commonwealth Bureau of Meteorology, Australia. The Southern Hemisphere surface pressure analyses are nearly hemispheric in scope, but where blank they are filled in subjectively by a combination of extrapolation and climatology. Geopotential heights are therefore determined at the following levels: 700 mb, 500 mb, 300 mb, 200 mb, 100 mb, 50 mb, 30 mb, and 10 mb. In this study only thickness (temperature) information above 100 mb and geopotential height information at and above 100 mb is used.

3. Technique used to calculate vertical motions

The technique used here to calculate the zonally-averaged vertical motion is similar to that used by Mahlman (1966) for the Northern Hemisphere with conventional data. It is basically the thermodynamic technique integrated around latitude circles. The total derivitive of potential temperature (θ) is expanded to give

$$\frac{d\theta}{dt} = \frac{\partial\theta}{\partial t} + \mathbf{V}_p \cdot \nabla\theta + \omega \frac{\partial\theta}{\partial p} , \qquad (1)$$

where $\mathbf{V}_p$ is vector horizontal wind on a surface of constant pressure, and ω is the vertical velocity in pressure coordinates. Expansion of the advection term in equation 1 gives

$$\frac{d\theta}{dt} = \frac{\partial\theta}{\partial t} + \nabla \cdot \mathbf{V}_p\theta - \theta\nabla \cdot \mathbf{V}_p + \omega \frac{\partial\theta}{\partial p} , \qquad (2)$$

Rearrangement of the terms gives

$$\left(-\frac{\partial\theta}{\partial p}\right)\omega = \frac{\partial\theta}{\partial t} - \frac{d\theta}{dt} + \nabla\cdot\mathbf{V}_p\theta - \theta\nabla\cdot\mathbf{V}_p \ , \tag{3}$$

Next, equation 3 is integrated over the area bounded by two latitudes ϕ_1 and ϕ_2, in this study usually 10° apart.

$$\int_{\phi_1}^{\phi_2}\left[-\frac{\partial\theta}{\partial p}\omega\right]_\lambda \cos\phi\, d\lambda = \int_{\phi_1}^{\phi_2}\left[\frac{\partial\theta}{dt}\right]_\lambda \cos\phi\, d\phi - \int_{\phi_1}^{\phi_2}\left[-\frac{d\theta}{dt}\right]_\lambda \cos\phi\, d\phi$$

$$+ \frac{1}{a}\left\{\cos\phi_2\ [v_{\phi_2}\theta]_\lambda - \cos\phi_1\ [v_{\phi_1}\theta]_\lambda\right\}$$

$$- \int_{\phi_1}^{\phi_2}[\theta\nabla\cdot\mathbf{V}_p]_\lambda \cos\phi\, d\phi \ , \tag{4}$$

where a is the Earth's radius and $[\ ]_\lambda$ implies averaging around a latitude circle.

The averaged quantities in the last two terms of equation 4 are expanded to give

$$[v\theta]_\lambda = [v]_\lambda[\theta]_\lambda + [(v)_\lambda(\theta)_\lambda]_\lambda \tag{5}$$

$$[\theta\nabla\cdot\mathbf{V}_p]_\lambda = [\theta]_\lambda[\nabla\cdot\mathbf{V}_p]_\lambda + [(\theta)_\lambda\ (\nabla\cdot\mathbf{V}_p)_\lambda]_\lambda \tag{6}$$

where

$$[\theta]_\lambda[\nabla\cdot\mathbf{V}_p]_\lambda = \frac{1}{2\pi}[\theta]_\lambda\int_0^{2\pi}\nabla\cdot\mathbf{V}_p d\lambda \ . \tag{7}$$

Substituting equations 5 and 6 into equation 4, and using 7 results in

$$\int_{\phi_1}^{\phi_2}\left[-\frac{\partial\theta}{\partial p}\,\omega\right]_\lambda \cos\phi\, d\phi = \int_{\phi_1}^{\phi_2}\left[\frac{\partial\theta}{\partial t}\right]_\lambda \cos\phi\, d\phi - \int_{\phi_1}^{\phi_2}\left[-\frac{d\theta}{dt}\right]\cos\phi\, d\phi$$

$$+\frac{1}{a}\left\{\cos\phi_2[(v_{\phi_2})_\lambda(\theta)_\lambda]_\lambda - \cos\phi_1\,[(v_{\phi_1})_\lambda(\theta)_\lambda]_\lambda\right\}$$

$$+\frac{1}{a}\left\{\cos\phi_2[v_{\phi_2}][\theta]_\lambda - \cos\phi_1\,[v_{\phi_1}]_\lambda[\theta]_\lambda\right\} \quad (8)$$

$$-\frac{1}{2\pi}\int_{\phi_1}^{\phi_2}[\theta]_\lambda\int_0^{2\pi}\nabla\cdot\mathbf{V}_p\cos\phi\, d\lambda d\phi$$

$$-\int_{\phi_1}^{\phi_2}[(\theta)_\lambda(\nabla\cdot\mathbf{V}_p)_\lambda]_\lambda\cos\phi\, d\phi$$

In equation 8 the second and third lines represent the effect of the divergence of the eddy flux and of the mean motion flux, respectively. The fourth and fifth lines represents the effect of divergence.

The last term in equation 8 involves the correlation of θ and $\nabla\cdot vp$ and is assumed small. The second-to-last term in equation 8 is well approximated by

$$-\frac{1}{2\pi}\int_{\phi_1}^{\phi_2}[\theta]_\lambda\int_0^{2\pi}\nabla\cdot\mathbf{V}_p\cos\phi\, d\phi\, d\lambda \cong -\frac{1}{2\pi}[\theta]_{\lambda,\phi}\int_{\phi_1}^{\phi_2}\int_0^{2\pi}\nabla\cdot\mathbf{V}_p\cos\phi\, d\phi\, d\lambda \quad (9)$$

where $[\theta]_{\lambda,\phi}$ is the average potential temperature for the area between ϕ_1 and ϕ_2. The right side of equation 9 is integrated to obtain

$$-\frac{1}{2\pi}[\theta]_{\lambda,\phi}\int_{\phi_1}^{\phi_2}\int_0^{2\pi}\nabla\cdot\mathbf{V}_p\cos\phi\, d\phi\, d\lambda = -\frac{1}{a}[\theta]_{\lambda,\phi}\left\{\cos\phi_2[v_{\phi_2}]_\lambda - \cos\phi_1[v_{\phi_1}]_\lambda\right\} \quad (10)$$

Neglecting the last term in equation 8 and using the right side of equation 10 to replace the second-to-last term gives

$$\int_{\phi_1}^{\phi_2}\left[-\frac{\partial\theta}{\partial p}\,\omega\right]_\lambda \cos\phi\, d\phi = \int_{\phi_1}^{\phi_2}\left[\frac{\partial\theta}{\partial t}\right]_\lambda \cos\phi\, d\phi - \int_{\phi_1}^{\phi_2}\left[-\frac{d\theta}{dt}\right]_\lambda \cos\phi\, d\phi$$
$$+ \frac{1}{a}\left\{\cos\phi_2\,[(v_{\phi_2})_\lambda(\theta)_\lambda]_\lambda - \cos\phi_1[(v_{\phi_1})_\lambda(\theta)_\lambda]_\lambda\right\}$$
$$+ \frac{1}{a}\left\{\cos\phi_2\,[v_{\phi_2}]_\lambda[\theta]_\lambda - \cos\phi_1[v_{\phi_1}]_\lambda[\theta]_\lambda\right\} \quad (11)$$
$$- \frac{1}{a}[\theta]_{\lambda,\phi}\left\{\cos\phi_2[v_{\phi_2}]_\lambda - \cos\phi_1[v_{\phi_1}]_\lambda\right\}$$

The last two lines in equation 11 are of opposite sign and are nearly, but not quite, equal. With a temperature gradient of 10°K/10° latitude and with θ approximately 200°K, $[\theta]_{\lambda,\phi}$ is different from either θ at ϕ_2 or θ at ϕ_2 by only about two or three percent. Thus the last two lines in equation will tend to cancel and their sum is negligible.

The integrals in equation 11 are evaluated, for example, by the approximation

$$\int_{\phi_1}^{\phi_2}\left[\frac{\partial\theta}{\partial t}\right]_\lambda \cos\phi\, d\phi \cong \left[\frac{\partial\theta}{\partial t}\right]_\lambda \cos\left(\frac{\phi_1+\phi_2}{2}\right)(\phi_2-\phi_1), \quad (12)$$

where $\left[\frac{\partial\theta}{\partial t}\right]_\lambda$ is evaluated at latitude $\frac{\phi_1+\phi_2}{2}$. With the last two lines eliminated as negligible and with the approximations exampled by equation 12, equation 11 becomes

$$\left[-\frac{\partial\theta}{\partial p}\omega\right]_\lambda = \left[\frac{\partial\theta}{\partial t}\right]_\lambda - \left[\frac{d\theta}{dt}\right]_\lambda$$

$$+ \left\{a\cos\left[\frac{\phi_1 + \phi_2}{2}\right](\phi_2 - \phi_1)\right\}^{-1} \left\{\cos\phi_2 \left[(v_{\phi_2})_\lambda (\theta)_\lambda\right]_\lambda \right.$$

$$\left. - \cos\phi_1 \left[(v_{\phi_1})_\lambda (\theta)_\lambda\right]_\lambda\right\} \qquad (13)$$

Equation 13 is used to calculate the zonally-averaged vertical motion.

4. Northern and Southern Hemisphere Vertical motion patterns

The static stability, local temperature change and heat flux convergence can be evaluated from the satellite-derived thickness and height fields. The local change term is of the order of 0.1°K/day, while the heating due to the flux convergence is of the order of 1°K/day in polar latitudes. The diabatic term is evaluated by using heating rates computed by Rodgers (1967) from climatological data. The term $\frac{d\theta}{dt}$ is negative everywhere during the polar night in the stratosphere, and is of the order of 1°K/day. Because the diabatic heating term varies less with latitude than the flux divergence term, the latter is most important in determining latitudinal variability of ω. For this reason the enthalpy flux as a function of latitude is examined.

Figure 1 shows the poleward heat flux in the 10-30 mb layer averaged over January 1970 for the Northern Hemisphere and over July 1969 for the Southern Hemisphere. Both SIRS and NMC curves are presented for the Northern Hemisphere. The geostrophic approximation is used for these computations. In both hemispheres the peak poleward flux is reached at 60°. It should be remembered that the polar vortex in the Northern

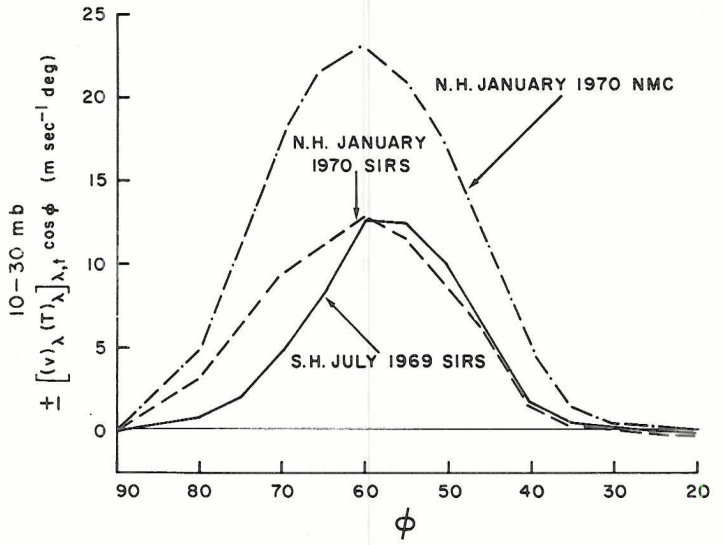

Fig. 1. Poleward heat flux in the 10-30 mb layer-January 1970 in the N. H., July 1969 in the S. H.

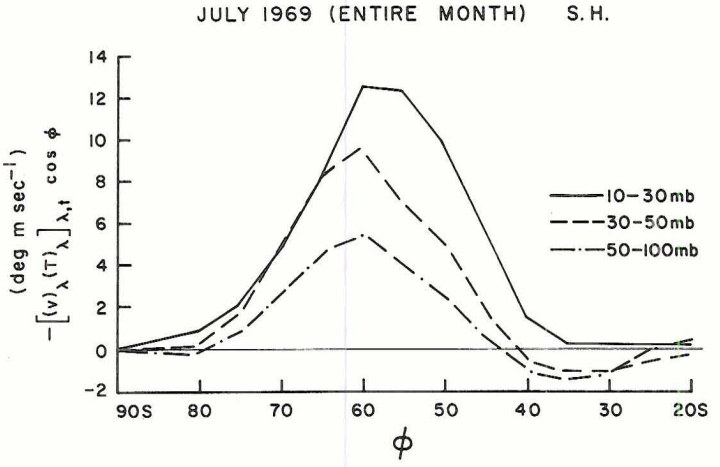

Fig. 2. Poleward heat fluxes in the stratosphere of the S. H. for July 1969.

Hemisphere broke down in early January that year. Thus the Northern Hemisphere curves may not be representative of normal (non-breakdown) conditions. The two SIRS curves peak at almost exactly the same value. The total flux convergence between 60° and the pole is about equal in the two hemispheres. However, the shape of the two curves is different. The Southern Hemisphere curve shows the flux decreasing very rapidly just poleward of 60°S and gradually levelling out. The greatest flux convergence is in the area between 60°S and 75°S. The Northern Hemisphere curve has a relatively constant decrease with latitude, indicating that the flux convergence is spread out more uniformly than that in the Southern Hemisphere. This difference in shape of the enthalpy flux curves is also evident in the 30-50 mb and 50-100 mb layers, but it is not so obvious.

The enthalpy flux distributions for all three layers for the Southern Hemisphere July 1969 are given in figure 2. In all three layers there is a rapid decrease in the flux poleward of the peak, then a flattening out of the curve in very high latitudes. The poleward enthalpy flux at 80°S in the 50-100 mb layer is slightly negative, meaning that between 80°S and the pole there is a flux divergence. The flux in the 30-50 mb layer at 80°S is very small positive, so that in this layer the flux divergence term in equation 13 is very small. In the Northern Hemisphere there is substantial flux convergence between 80°N and the pole (see figure 1). Thus there is a significant difference between the hemispheres in the patterns of heat flux and heat flux convergence in the polar-night stratosphere.

The heat fluxes, the local change in temperature and the static stability can be determined from the SIRS-based structure. The diabatic

heating, $\frac{d\theta}{dt}$, is essentially entirely due to radiative heating or cooling, and can not be calculated without a knowledge of the vertical distribution of ozone. Even if the ozone distribution is known, the calculation is difficult. Rodgers (1967) has calculated tropospheric and stratospheric radiative cooling rates from climatological data in the Northern Hemisphere. No such computations are available for the Southern Hemisphere. Table 2 gives the values of $\frac{d\theta}{dt}$ (adapted from Rodgers (1967)) used in this study as a function of latitude and layer. Identical values are used in each hemisphere. Rodgers only extended his calculations

	Latitude				
	80°	70°	60°	50°	50°
10-30 mb	-1.2	-1.2	-1.0	-0.8	-0.5
30-50 mb	-0.9	-0.9	-0.8	-0.6	-0.3
50-100 mb	-0.6	-0.6	-0.5	-0.4	-0.2

Table 2 Values of $\frac{d\theta}{dt}$ used in vertical motion calculations. (Based on Rodgers (1967) calculations) Units: °C/day.

to 70°N. This author assumes that the values at 70° hold at all latitudes poleward of 70°. The values in Table 2 for the 10-30 mb layer are from Rodgers' calculations at 20 mb, the values for the 30-50 mb layer are an average of the 30 mb and 50 mb calculations, and the values for the 50-100 mb layer are from Rodgers' calculation for 70 mb. In applying these cooling rates to the Southern Hemisphere the author is assuming that there is no substantial difference in the actual rates between the hemispheres.

The results of evaluating the terms in equation 13 and solving for ω in the Northern Hemisphere for January 1970 with both NMC and SIRS-based structure are shown in figures 3a and b. The NMC-based calculation (3a)shows rising motion in high latitudes and sinking in low latitudes. The axis of rising motion slopes poleward with height and the maximum rising motion is located at 20 mb at the pole. The pattern of rising motion over the pole and sinking in mid-latitudes is typical of patterns found by other authors (e.g., Mahlman, 1966) for the Northern Hemisphere. Mahlman (1966) also showed that this pattern of rising and sinking motion occurs before, during and after breakdowns. Miller, Brown and Campana (1972) using the quasi-geostrophic, adiabatic omega equation obtain a cross-section of ω for the period 1-15 January 1970 which also indicates the same general pattern of ascent and descent as in figure 3a. Thus the use of equation 13 and NMC structure appears to produce a cross-section of vertical motion in the stratosphere which closely resembles previous estimates made for different years, and also resembles a calculation made for the same year.

Figure 3b is the vertical motion pattern for the Northern Hemisphere calculated using the heat fluxes, local temperature changes and static stability derived from the SIRS-based structure. There are some similarities and some differences between figures 3a and b. In figure 3b there is rising motion over the pole in the higher layers and sinking motion in midlatitudes. There is also a small area of rising motion at 60°N at 75 mb. The maximum rising motion is found at or near the pole and in the top layer (10-30 mb). However the volume of rising motion is much less than that shown in figure 3a. Magnitudes of maximum rising and sinking motions are underestimated.

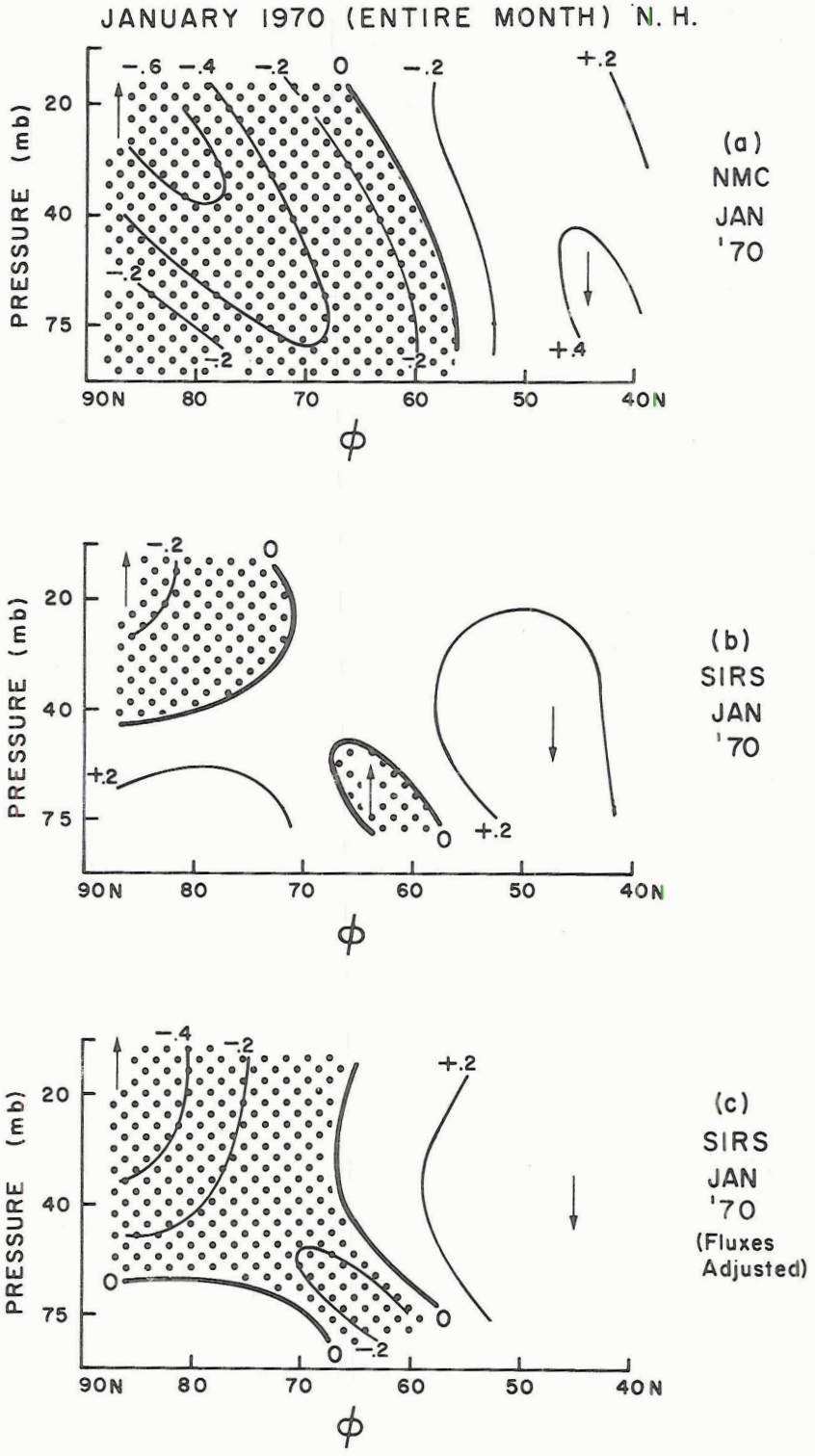

Fig. 3. Zonally-averaged vertical motion patterns for the N. H. for January 1970. Units: mb/day. Stippled area denotes area of ascent.

The main factor in the difference between figures 3a and b is the underestimation of eddy heat fluxes in the SIRS-based calculation. This underestimation is evident in figure 1. Although the SIRS-based curve underestimates the magnitude of the actual fluxes, it reproduces the shape of the NMC curve and the locations of flux divergence and convergence. This is also true for the two lower layers (30-50 mb and 50-100 mb). The underestimation by the SIRS-based fluxes varies with latitude and between layers. The minimum underestimation between 45°N and 75°N is 56 per cent. To at least partially correct for the underestimation, a factor of 1.8 (based arbitrarily on the 56 per cent figure) is applied to the SIRS-based flux values and the vertical motion computation redone. The results are shown in figure 3c. The general rising motion in high latitudes at high levels and the sinking motion in mid-latitudes are still present. The region of rising motion has expanded and indicates the slope with height of the NMC-based cross-section. Magnitudes of maximum rising and sinking motion are also in closer agreement. The adjustment factor of 1.8 as based on the minimum underestimation is chosen because the author believes that the larger underestimations present, especially in the lower layers, are due to the low density of satellite radiance data in the Northern Hemisphere for January 1970 relative to the density of observations over the Southern Hemisphere in July 1969, the Southern Hemisphere winter month to be examined.

The results of the vertical motion calculations for the Southern Hemisphere for July 1969 are shown in figures 4a and b. Part a of the figure is based on fluxes calculated directly from the SIRS-based structure and part b is based on calculations made with the fluxes adjusted by the factor of 1.8. Both parts of figure 4 show an area of

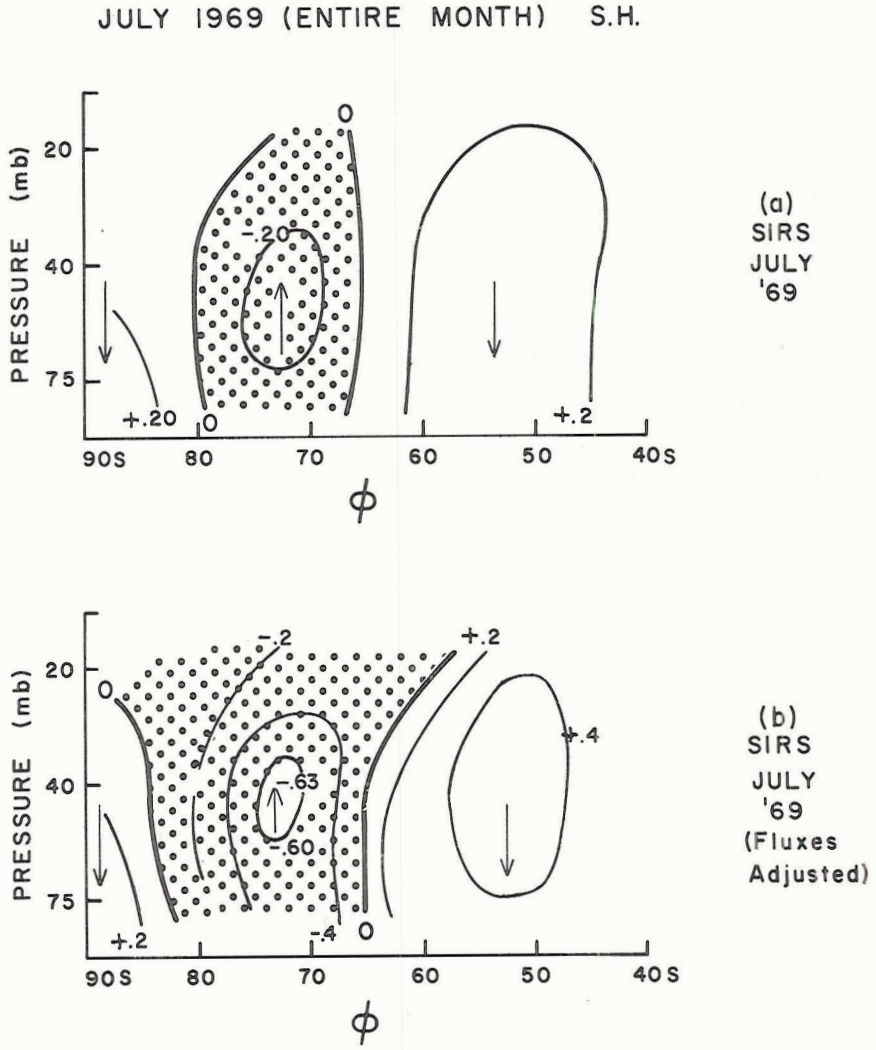

Fig. 4. Zonally-averaged vertical motion patterns for the S. H. for July 1969. Units: mb/day.

descending motion centered at 50°S, an area of ascent centered at about 73°S and area of descent over the South Pole. With the assumption of ascent in low latitudes (<30°S), figure 4 indicates a three-celled meridional circulation compared to the two-celled structure in the Northern Hemisphere. The predominant sinking motion over the Southern Hemisphere pole has been previously postulated by Reiter (1969, 1971) on the basis of ozone measurements over Antarctica. Since Rubin and Weyant (1963) have already noted a general subsidence below 75 mb to the surface over the South Pole it is evident that ozone-rich air in the lower stratosphere is transported downward to the surface to produce the midwinter peaks in surface ozone observed over Antarctica (Wisse and Meerburg, 1969).

5. Southern Hemisphere variations during July 1969

The early part of July 1969 was characterized by a midwinter minor warming in the Southern Hemisphere stratosphere (Fritz and Soules, 1970; Miller, Finger and Gelman, 1970). Except for the last few days, the remainder of the month was relatively quiet. The vertical motion patterns during the minor warming and during the quiet period exhibit significant differences. The meridional circulation for 1-10 July 1969 (during the minor warming) is given in figures 5a and b. The pattern for 18-27 July 1969 (quiet period) is given in figures 6a and b. During 1-10 July the descending branch over the South Pole disappears and the ascending and descending branches at about 70°S and 50°S respectively have larger magnitudes than the monthly averages in those locations. Even though the descending branch over the pole disappears, the ascending branch is still centered between 70°S and 75°S. During the quiet period (18-27 July 1969) the vertical motion pattern shows very strong descent over

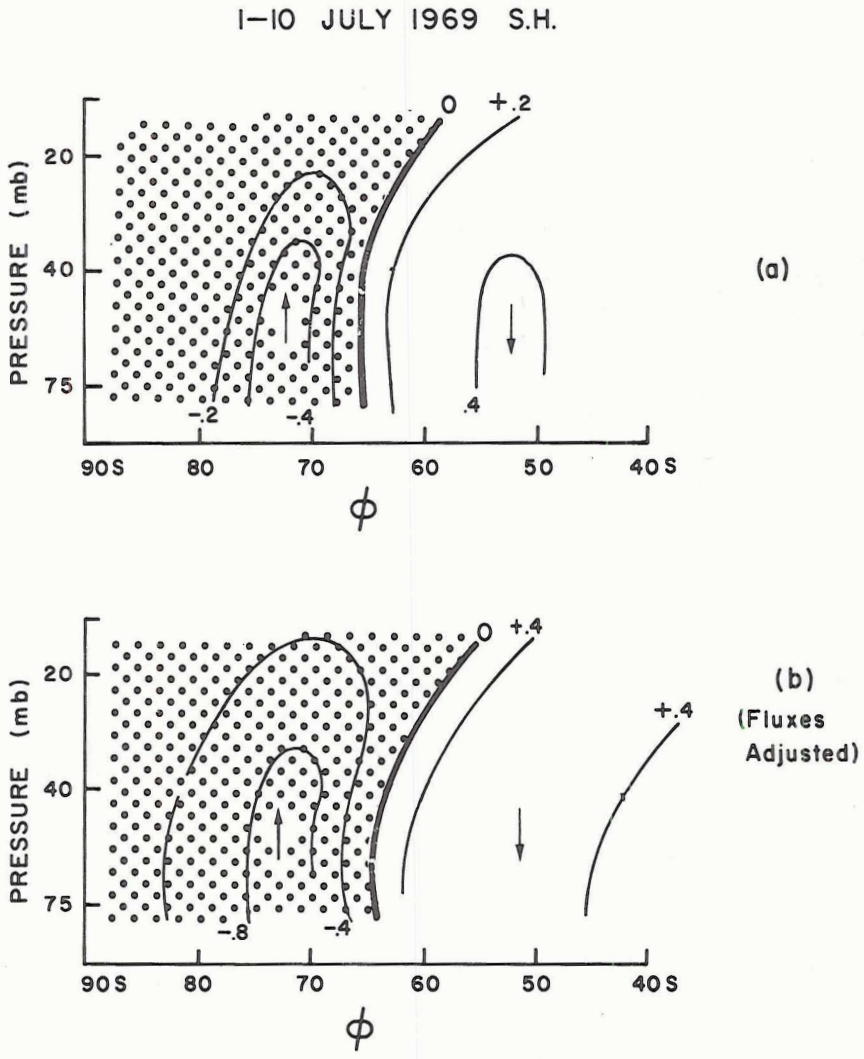

Fig. 5. Zonally-averaged vertical motion patterns for the S. H. for the period 1-10 July 1969, during a minor mid-winter warming. Units: mb/day.

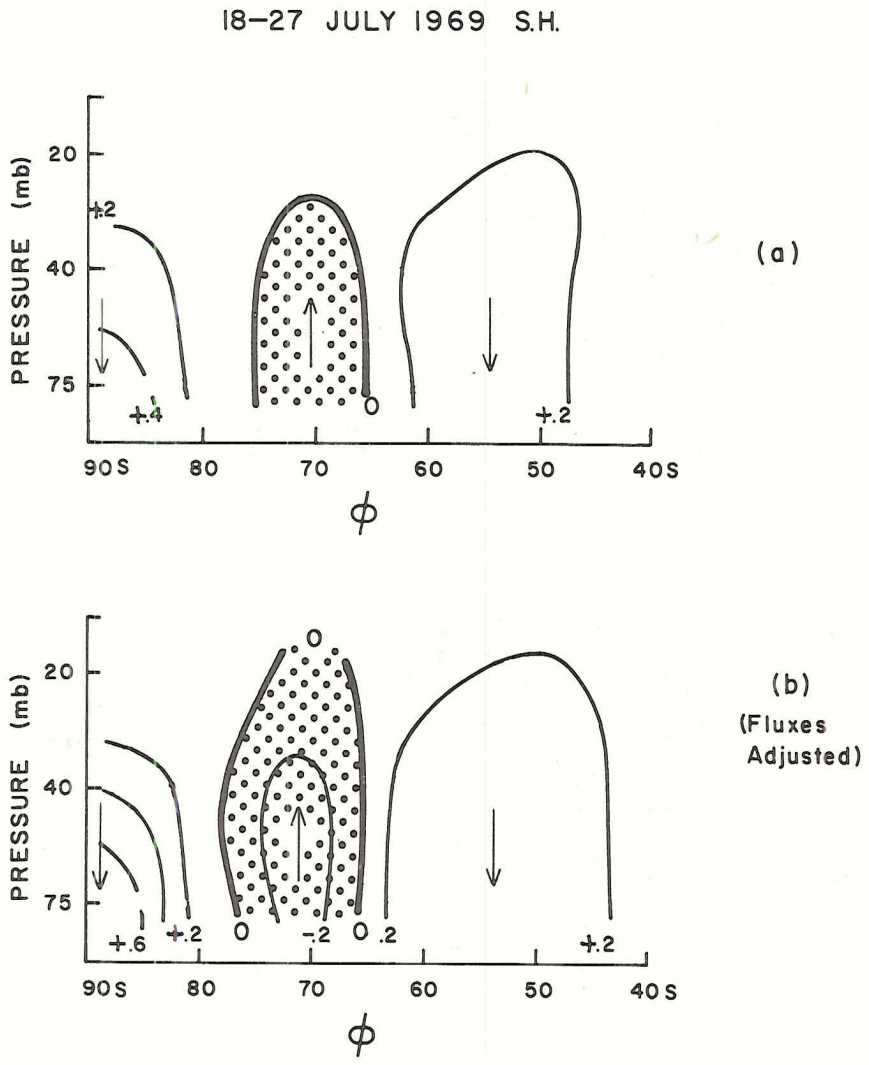

Fig. 6. Zonally-averaged vertical motion patterns for the S. H. for the period 18-27 July 1969, a quiet period. Units: mb/day.

the pole (figure 6a and b). According to figure 6b the descending motion covered the area poleward of about 78°S with maximum downward velocity occurring in the lowest layer of calculation. The ascending branch at 70°S and the descending branch farther equatorward are less intense than the monthly average (figure 4) and much less intense than during the minor warming (figure 5). Thus during minor warmings in the Southern Hemisphere it appears that the descending branch over the pole disappears. This disappearance may have consequences in the distribution of total and surface ozone over Antarctica. The 18-27 July quiet period is probably more typical of normal conditions during the Southern Hemisphere winter.

The difference in vertical motion patterns between the periods 1-10 July and 18-27 July 1969 is closely related to the eddy heat flux distributions for those two periods. These distributions are shown in figures 7a and b. The peak fluxes during 1-10 July are approximately three times as great as those for the 18-27 July period. Thus the flux divergences on either side of the peak are also about three times as great. In very high latitudes another important difference is that although both the 50-100 mb and 30-50 mb layers exhibit eddy flux divergence between 80°S and 90°S during the period 18-27 July, all layers exhibit flux convergence in that location for the 1-10 July period. This is the reason for the existence of the difference in vertical motion patterns over the pole between the two periods.

Fritz and Soules (1970) examine a number of Southern Hemisphere stratospheric temperature fluctuations during the fall, winter and spring of 1969 using SIRS channel 8 data. Between 25 June and 10 July they indicate a large increase in channel 8 radiance in the southern polar

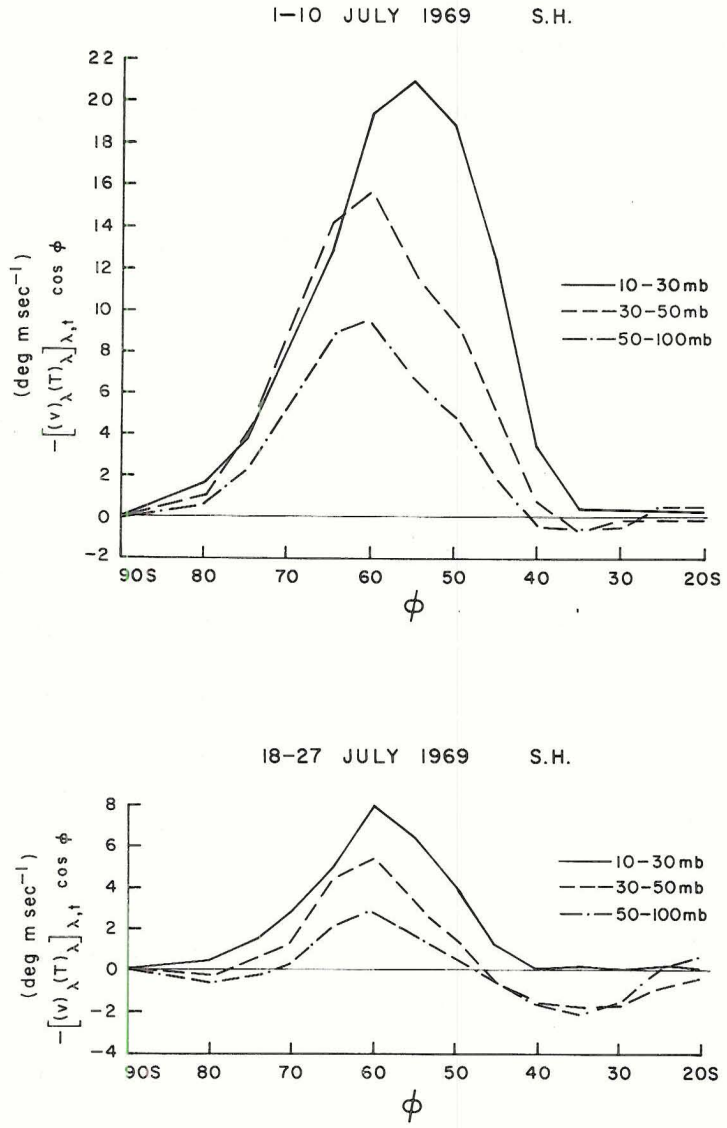

Fig. 7. Poleward heat fluxes in the S. H. during the periods 1-10 July and 18-27 July 1969.

regions. Accompanying the warming (increasing radiance) in the high latitudes of the Southern Hemisphere, they also find decreasing radiance (cooling) in Southern Hemisphere low latitudes and in the Northern Hemisphere. The early July case is just one of several similar compensating changes noted by Fritz and Soules. In this section it has been noted that there are significant differences in the eddy flux of enthalpy patterns and in the mean meridional motion patterns between the time of the early July warming (1-10 July) and the quiet period (18-27 July). These observations support the Fritz and Soules postulate that irregular (non-seasonal) fluctuations in stratospheric temperature are related to changes in the large-scale eddies and/or changes in the mean meridional circulations.

6. Conclusions

In this study zonally-averaged vertical motions in the stratosphere of both hemispheres during winter have been calculated using atmospheric structure derived from satellite radiance measurements. The calculations reconfirm the work by previous authors that the Northern Hemisphere has a two-celled structure with rising motion over the pole and at low latitudes and sinking motion in mid-latitudes. The Southern Hemsiphere stratosphere, however, has a three-celled structure with sinking over the pole and in mid-latitudes and ascending branches at about at 70°S and in low latitudes.

The Southern Hemisphere vertical motion patterns are significantly different during a time of a minor midwinter warming and during a quiet period. During the minor midwinter warming the descending branch over the pole disappears and the ascending and descending branches at about 70°S and 50°S, respectively are strong. During the quiet period the descending branch over the pole is strong while the lower latitude branches are relatively weak.

REFERENCES

1. Fritz, S. and S. D. Soules, 1970: Large-scale Temperature Changes in the Stratosphere Observed from Nimbus III, J. Atmos. Sci., 27(7): 1091-1097.

2. Julian, P. R. and K. Labitzke, 1965: A Study of Atmospheric Energetics During the January-February 1963 Stratospheric Warming, J. Atmos. Sci., 22(6): 597-610.

3. Mahlman, J. D., 1966: Atmospheric General Circulation and Transport of Radioactive Debris, Atmospheric Science Paper No. 103, Colorado State University.

4. Miller, A. J., J. A. Brown and K. A. Campana, 1972: A Study of the Energetics of an Upper Stratospheric Warming (1969-1970), Quart. J. R. Met. Soc., 98: 730-744.

5. Miller, A. J., F. G. Finger and M. E. Gelman, 1970: 30 mb Synoptic Analyses for the 1969 Southern Hemisphere Winter Derived with the Aid of Nimbus III (SIRS) Data, NASA TMX-2109, Washington, D. C., 27 pp.

6. Reed, R. J., J. Wolfe and H. Nishimoto, 1963: A Spectral Analysis of the Energetics of the Stratospheric Sudden Warming of Early 1957, J. Atmos. Sci., 20(4): 256-275.

7. Reiter, E. R., 1969: Atmospheric Transport Processes, Part I: Energy Transfers and Transformations, USAEC Report TID-24868.

8. Reiter, E. R., 1971: Atmospheric Transport Processes, Part II: Chemical Tracers, USAEC Report TID-25314.

9. Rodgers, C. D., 1967: The Radiative Heat Budget of the Troposphere and Lower Stratosphere, Report No. A2, Massachusetts Institute of Technology.

10. Rubin, M. J. and W. Weyant, 1963. The Mass and Heat Budget of the Antarctic Atmosphere, Mon. Weather Rev. 91(10-12): 487-493.

11. Smith, W. L., H. M. Woolf and W. J. Jacob, 1970: A Regression Method for Obtaining Real-Time Temperature and Geopotential Height Profiles from Satellite Spectrometer Measurements and its Applications to Nimbus III SIRS Observations, Mon. Weather Rev., 98(8): 582-603.

12. Wisse, J. A. and A. J. Meerburg, 1969: Ozone Observations at Base Kins Baudouin in 1965 and 1966, Arch. Meteorol. Geophys. Bioclimatol., Ser. A, 18(1-2): 41-54.